**Article:**

Adhikari, A., Gilroy, E.R., Hayward, T.J. et al. (1 more author) (2021) Surface acoustic wave assisted depinning of magnetic domain walls. Journal of Physics: Condensed Matter, 33 (31). 31LT01. ISSN 0953-8984

https://doi.org/10.1088/1361-648x/ac02e4

# Surface acoustic wave assisted depinning of magnetic domain walls

A. Adhikari,[1] E.R. Gilroy[2], T.J. Hayward[2] and S. Adenwalla,[1]

[1]Department of Physics and Astronomy and Nebraska Center for Materials and Nanoscience, University of Nebraska-Lincoln, Lincoln, Nebraska 68588, USA

[2]Department of Materials Science and Engineering, University of Sheffield, Sheffield, UK

*We investigate the effects of high frequency strain on the depinning of magnetic domain walls in perpendicular anisotropy materials. Micron wide stripes of [Co(0.3nm)/Pt(0.6nm)]$_5$ are patterned between a pair of identical inter-digital transducers that generate high frequency (114.8 MHz) standing surface acoustic waves. We use magneto-optical Kerr effect microscopy to characterize the thermally-assisted depinning of domain walls at defect sites within the strips. Our results show that the excitation of the domain walls with surface acoustic wavs results in an increase in their depinning probabilities by approximately a factor of 10. Our data are consistent with a model in which the magnetoelastic anisotropies induced by the acoustic waves modulate the energy barriers that pin the domain walls. These results suggest an alternative route to domain wall depinning in thin films and nanostructures and are relevant to the development of racetrack memories, where domain wall pinning can result in reduced velocities and non-deterministic motion.*

The paths of magnetic domains walls (DWs) are rarely smooth, strewn with a variety of impediments. In spite of this, high average speeds of >1500 m/s in permalloy nanowires with in-plane anisotropy have been achieved [1]. The development of racetrack electronics [2] based on ferromagnetic DWs has turbocharged research on DW depinning and dynamics. Perpendicular magnetic anisotropy (PMA) materials such as Co/Pt [3], [4], Co/Ni [5], [6], Co/Pd [7], Co/AlO$_x$ and CoB/TaO$_x$ [8] are promising candidates for DW based memories with narrow DWs, stable magnetic states and high DW velocities. However, the narrow widths result in greater susceptibility to even small pinning barriers. Magnetic fields [1], [9] and currents [9], [10] have been shown to depin DWs and result in high DW velocities, but both have high power requirements. Circularly polarized laser pulses can also assist DW motion [6] depending on the chirality of the DW, but once again require fairly high power.

Strain fields offer an alternative driver of domain wall motion and depinning. DC strains in thin film ferromagnets reveal a slight increase in DW velocity [11] and tune spin wave switching in lateral [12] or bilateral [13] yttrium iron garnet (YIG) magnonic stripe(s). Mechanically strained [14] Pt/Co/Pt trilayers show changes in the DMI constant, both along and perpendicular to the strain direction.

SAW in magnetic thin films [15] can drive changes in the magnetization direction [16], [17], increase DW velocities [18], [19] and decrease coercive fields [18], [20], [21]. Out-of-plane films of (Ga,Mn)(As,P) show SAW driven precessional [22] switching from up to down, highly dependent on the local coercivity and the rf pulse length. SAW in Ni nanowires [23] substantially assist in magnetization switching and provide an rf effective magnetic field that depends on the orientation of magnetization, an attractive option for moving DWs [24] and in spin current generation at microwave frequencies [25]. Micromagnetic simulations, together with an analytic model [26] show that depinned DW are driven most strongly by the strain gradient.

In this paper, we investigate the effects of SAW on DW depinning from deep pinning sites. Depinning is a thermally activated Arrhenius-like stochastic process [27], [28] and so we make repeated measurements of depinning as a function of pulse width, magnetic field and SAW intensities to fully characterize the strength of the pinning sites and the depinning behavior. This is fundamentally different from [19] which measured DW motion in the creep regime, averaging over multiple weak pinning sites. In contrast, this work investigates the effects of SAW on individual strong pinning sites.

The sample, shown in Figure 1(a) consists of sputtered thin films of Cr(2nm)/Pt(2nm)/[Co(0.3nm)/ Pt(0.6nm)]$_5$ on 128° Y cut lithium niobate ($LiNbO_3$). Two identical inter-digital transducers (IDTs) with wavelength $\lambda = 32\ \mu\text{m}$ and frequency $f_0 = 114.8$ MHz generate standing SAW across a series of stripes that are parallel to the x-axis propagation direction. The innermost fingers of the two IDTs are separated by $15\lambda$. The 32 μm wavelength of the SAW standing wave is many orders of magnitude larger than the typical domain wall width of a few nm [29], [30] so that SAW generated strains remain essentially uniform over the width of a DW. The 240 μm long stripes with widths of 4μm ($S_1$, $S_2$, $S_3$, $S_4$), 3μm ($S_5$, $S_6$, $S_7$, $S_8$) and 5μm ($S_9$, $S_{10}$) are connected to large area domain reservoirs. Patterning was accomplished using photolithography, followed by argon ion milling at a base pressure of $3\times10^{-8}$ Torr, with ion energy of 300V and a beam current of 100mA for 4 minutes. Ion milling is known to result in deep pinning sites and these are randomly distributed along the stripes [31].

All data shown here are based on measurements of three representative stripes-$S_6$ (3μm wide), $S_3$ (4μm) and $S_9$ (5μm), with the choice(s) based on the domain nucleation position and the presence of a variety of pinning sites. Domain nucleation for stripe $S_3$ ($S_6$) occurs in the left (right) reservoir. For stripe $S_9$ the nucleation point is close to the right reservoir. DW motion was measured in a MOKE microscope that incorporated a homemade solenoid with a tapered pole piece for out-of-plane fields and a 480×640 pixel COMS camera (Celestron). All measurements were made using a 20x objective lens resulting in a spatial resolution per pixel of ($0.38\times0.38\ \mu m^2$). All images were subtracted from a reference image of a magnetically saturated sample at a field of $\pm$800 Oe. An oppositely directed field slightly lower than the coercive fields (205 Oe) nucleated a magnetic DW. Up to 100 magnetic pulses at a variety of fields and pulse widths, with and without SAW excitation drove domain wall motion. The images were captured and processed using MATLAB [32], averaging over 10 images to improve signal to noise, and the application of a median filter and subtraction of the reference image to improve domain contrast. The positions of DWs were defined as the average of line profiles along the stripe. IMAGEJ [33] was used to scale the images. The hysteresis loops (Figure 1(d)) for each stripe were measured using the relative areas of up and down domains as a measure of the net magnetization. The small step in the $S_3$ loop can be ascribed to a strong pinning site.

Figures 2(a), (b) and (c) offer a snapshot of our experiments on the 3μm wide stripe ($S_6$) allowing for a direct, quantitative comparison of the depinning behavior as a function of pulse width, magnetic field and SAW amplitude. Each trace is the result of a single measurement. The pinning sites are the horizontal plateaus in the DW motion, labeled $P_1$-$P_4$. Increases in the pulse width (Figure 2(a)), magnetic field (Figure 2(b)) and SAW voltage (Figure 2(c)) all result in more efficient depinning. Strong pinning sites require repeated applications of a pulse to depin DWs (e.g. $P_3$ at $x\approx98\mu m$) while weak pinning sites ($P_2$) require fewer pulses to depin, so, for example, we can see that $P_2$ is weaker than $P_3$. Shorter pulses (down to 1ms) and lower fields reveal even the weakest pinning sites, mapping the pinning sites with greater precision whereas the longer pulse widths sweep the DW smoothly through the pinning sites.

Similar measurements for different stripe widths shown in supplementary Figure S1 indicate that the pinning positions are highly reproducible. The variation in pinning strength indicates the presence of extrinsic defects and do not correlate with measurements of edge roughness. Ion milling is known to introduce defects that result in strong pinning sites [31] and we attribute the pinning sites in these stripes to the effects of the high energy ions.

A SAW voltage of 3V results in a 10-20 fold drop in the average depinning times for all 8 pinning sites, corresponding to an applied field increase of approximately 20%. For example, in a single trial, the number of 1ms long 166 Oe field pulses required to depin the DW at $P_3$ in Figure 2(c) drops from 44 in the *absence* of SAW to 4 with a 3V SAW excitation. Similar behavior is seen at all pinning sites. SAW also increases the velocity of DWs [18], [19] in regions between the strong pinning sites, with a greater than 2 fold increase in velocity at a SAW voltage of 3V, as shown in Supplementary Figure S2. The rest of the manuscript *quantifies* the DW depinning probability, $P(t, H, V_{SAW})$, as a function of pulse width, magnetic field and SAW amplitude,

Because DW depinning is a thermally activated Arrhenius-like stochastic process [27], [28], we make repeated measurements at each field, pulse width and/or SAW voltage. The depinning probability $P(t)$ as a function of variable pulse widths that range from 1 ms to 1 second at a fixed field value allows for a quantitative comparison of the relative strengths of the pinning sites. The variation in pulse width defines a depinning probability as a function of time for a fixed field value, with the depinning probability $P(t)$ for a particular pulse width obtained by counting the number of pulses, $n$, required to depin, where $P(t) = 1/n$. These measurements are repeated at least 5 times for each pulse width, and the averaged probability for a representative group of weak ($P_2$), intermediate ($P_3$) and strong ($P_6$) pinning sites is shown in Figure 3(a) at a fixed field value of 205 Oe. All pinning sites show the expected exponential dependence,

$$P(t) = 1 - e^{-t/\tau} \qquad (1)$$

where $t$ corresponds to the pulse width and $\tau$, the characteristic depinning time, is a function of the pinning potential $E_0$ (the energy barrier at $H = 0$), the temperature $T$ and the applied external field $H$ viz.

$$\tau = \tau_0 e^{\frac{E_0}{k_B T}\left(1 - \frac{H}{H_0}\right)} \qquad (2)$$

where $\tau_0$ is the reciprocal of the attempt frequency, $k_B$ is the Boltzmann constant and $H_0$ is the depinning field at $T = 0$ K (assuming an exponent of 1 in the Sharrock Equation [34]). Error bars indicate the standard deviation of the repeated measurements. The range of pulse widths, covering three orders of magnitude, allow for an accurate measure of the characteristic depinning time at $H = 205$ Oe, $\tau_{205}$, for each of the 8 pinning sites, which range (Figure 3(b)) from a high of $\tau =$ 1.4 s for the strongest pinning site ($P_6$ on the 4μm stripe), to a low of 0.03 s ($P_2$ on the 3μm stripe). The error bar for the strongest pinning site is large because the depinning time is longer than the longest pulse width.

Measurements of the field dependence of depinning, $P(t, H)$, (with 8 measurements at each field value) for a fixed pulse width of 1ms enables further characterization of the pinning sites. The characteristic depinning time at each field value, $\tau(H)$ is obtained from the probability using Equation (1) and is shown in Figure 3(c). From Equation (2), a plot of $Ln[\tau(H)]$ vs $H$ will be a straight line, with a slope of $\left(\frac{E_0}{k_B T}\right)\frac{1}{H_0}$ and an intercept of $\left(\frac{E_0}{k_B T} + ln[\tau_0]\right)$. Assuming a value of $\tau_0$ =0.1 ns, the values of $E_0$ and $H_0$ for 4 pinning sites are shown in Table 1. Note that variations in the choice of $\tau_0$ result in only small shifts in these values. A plot of $E_0$ vs. $\tau_{205}$ (Figure 3(d)) indicates that, within error bars, the two increase roughly in tandem.

The probability of depinning using pulsed magnetic fields in conjunction with SAW is denoted by $P(t, H, V_{SAW})$, and is measured using 5ms, $H = 205$ Oe field pulses, in the presence of a continuous SAW background at the resonance frequency of $f_0 = 114.8$ MHz. Increasing SAW voltages results in higher depinning probabilities, an effect seen for all pinning sites, (Figure 4(a)) with, for example, a 7-fold increase in the depinning probability at an applied voltage of 5V for pinning site $P_3$, (Figure 4(b) and 4(c)), equivalent to an additional out-of-plane field of ~35 Oe. SAWs in the absence of an applied field do not depin even the weakest DW. In general, SAWs at the highest voltage of 5V increase the depinning probability by a factor of somewhere between 4 to 9, depending on the pinning site, as shown in Figure 4(b). This SAW assisted increase in the depinning probability shows no dependence on either the strength or location of the pinning site, as seen in Figures 4(b) and 4(c) in which the increased probability P(5V)/P(0V) is plotted against $\tau_{205}$ (a measure of the pinning strength) and the distance from a node/antinode, respectively.

Because depinning is a thermally activated process, we look first to the possibility of SAW induced heating. If we assume the increased probability is due to thermal activation alone, the 4 to 9-fold SAW induced increase in the depinning probability corresponds to a minimum temperature increase of 20K. It is highly unlikely that SAW, even at the highest applied voltage of 5V, will result in such substantial heating. Calculations of the electrical characteristics of the IDTs at resonance (see Supplementary) indicate that the maximum power delivered to each IDT is 34 mW, corresponding to a power density of 50 mW/mm$^2$. A careful study of temperature effects in 128$^0$ Y-cut $LiNbO_3$ [35], using much high-power densities (0.5-3.5W/mm$^2$) indicate a shift in the resonance frequency of approximately 31.5 kHz/K; hence, with a FWHM $\Delta$f=0.07MHz, we are sensitive to resonance shifts corresponding to temperature changes as small as 3K. No shift in the resonance frequency has been observed.

| Defect Site | $E_0$ ($10^{-19}$ J) | $H_0$ (Oe) | $K_{defect}$ (MJ/m$^3$) | $l_y$ (nm) |
|---|---|---|---|---|
| $P_1$ | 1.92 | 368 | 0.303 | 11.5 |
| $P_2$ | 1.72 | 385 | 0.303 | 10.2 |
| $P_8$ | 1.49 | 518 | 0.302 | 8.9 |
| $P_3$ | 2.00 | 372 | 0.304 | 12.0 |

*Table 1: Fitted parameters for defect sites $P_1$-$P_3$ and $P_8$. Values of $\overline{E_0}$ and $\overline{H_0}$ are extracted from plots of pinning probability vs applied field, while the values of $K_{defect}$ and $l_y$ result from fitting the barrier modulation model to experimental measurements of depinning probability vs SAW voltage.*

Having demonstrated the ability of SAWs to assist depinning we present analytical modelling to explain the physical mechanisms underlying these phenomena. Any SAW driven depinning mechanisms in ferromagnets must result from the magnetoelastic term in the free energy. The x-propagating orientation of the IDTs results in a SAW wave with both longitudinal, $e_{xx}$, and shear, $e_{xy}$, strains with a ratio of $e_{xx}/e_{xy}$ ~20, so even though $B_2$, the 2nd order magnetostrictive constant, is larger than $B_1$ ($B_1 = -15.9 \times 10^6$ N/m$^2$ and $B_2 = 26.6 \times 10^6$ N/m$^2$ for fcc cobalt [36]) the shear free energy term is about an order of magnitude smaller than the longitudinal term. We approximate the remaining strain components $e_{xx}$and $e_{zz}$ to those of a SAW propagating through an isotropic medium [19]. Since the film is not constrained in the z direction ($\sigma_{zz}$=0), $e_{zz} = \frac{-\nu}{(1-\nu)} e_{xx}$ where $\nu$ is the Poisson ratio of the film/substrate combination, $\nu$~0.4 [37] and the leading magnetoelastic terms in the localized free energy density are:

$$E_{ME} = B_1 \left( e_{xx}\alpha_x^2 - \frac{\nu}{(1-\upsilon)} e_{xx}\alpha_z^2 \right) \sin(\omega t) \sin(kx) \quad (3)$$

where $\alpha_i$ are the directional cosines of the magnetization, $\omega = 2\pi f_0$, $e_{xx}$ represents the SAW's longitudinal strain amplitude, $k = \frac{2\pi}{\lambda}$ and $x$ is the position along the stripe. Noting that for a Bloch DW $\alpha_x = 0$ and for a Néel DW $\alpha_x^2 = 1 - \alpha_z^2$, a generalized form of Equation (3) may be written as:

$$E_{ME} = -B_1 e \alpha_z^2 \sin(\omega t) \sin(kx) \quad (4)$$

where $e = \frac{\nu}{(1-\upsilon)} e_{xx}$ for a Bloch DW or $e = e_{xx} + \frac{\nu}{(1-\upsilon)} e_{xx}$ for a Néel DW. (We neglect terms that have no dependence on magnetization direction). DWs in Co/Pt multilayers have been the subject of some debate. Lorentz microscopy images [38] indicate a circulating flux closure domain with no Bloch character. However, depinning measurements [39] indicate that a Bloch DW may acquire a Néel-like character if an in-plane field is applied. Moreover, strain has been shown to alter the direction of magnetization [17], [29], [30] within the DW, and can result in transformations between Néel and Bloch DWs. Hence, the assumption of purely Bloch or Néel DWs may be over simplified. In the following we will assume Néel DW structure for simplicity, but we would expect our results to be broadly similar for both Bloch DWs, and DWs with intermediate structure.

We assume that pinning sites are solely a result of a local decrease in the out-of-plane anisotropy from $K_1$ to $K_{defect}$ and model the pinning sites by trapezoidal energy wells with depth $E_0$ and width $l_x$ along the direction of DW propagation, $l_x > \pi\Delta$ where $\Delta$ is the DW width (Figure 5(a)). The defect site spans a distance $l_y$ in the direction of the stripe width $w$, and we assume it extends through the entirety of the stripe thickness $d$ (Figure 5(d)). The energy barrier against depinning is thus given by:

$$E_0 = l_y d\left(\sigma_{DW}(K_1) - \sigma_{DW}(K_{defect})\right) \quad (5)$$

where $\sigma_{DW}$ is the DW energy per unit area, calculated from the model of DeJong and Livesly [40].

Application of magnetic fields, $H$, along the z-axis result in a linear tilt of the DW's Zeeman energy and a reduced energy barrier $E_H$ (Figure 5(b)):

$$E_H = E_0 \left(1 - \frac{H}{H_0}\right) \quad (6)$$

where $H_0$ is the T = 0 depinning field, which is directly proportional to the gradient of the energy landscape at the edge of the well. Modulation of both anisotropies, $K_1$ and $K_{defect}$ by the SAW can modify $E_0$, but not the spatial extent of the energy well. The implication of this is that increases/decreases in $E_0$ result in proportional increases/decreases in $H_0$ (Figure 5(c)).

We consider two possible mechanisms for SAW assisted depinning: (i) generation of out-of-plane effective fields by magnetoelastic anisotropy gradients and (ii) modulation of DW pinning potentials by magnetoelastic anisotropies. In the following, we fit the data to simple models of each effect to explore whether they offer a credible explanation of our experimental data. Note that the rapidly oscillating strains require any SAW derived mechanism(s) for DW depinning be integrated over the cycle of the SAW excitation.

The first, arising from magnetoelastic gradients, results in a negligible change in the depinning probability as shown in Figure 6. The details of the calculations are shown in Supplementary Information. In all cases, the effective field model (which has no free parameters) produces effects that are far too small to explain the experimental results. Calculations of the maximum of $H_{eff}$ at maximum strain ($e = 1 \times 10^{-3}$) suggest that $H_{eff}$ < 1 Oe, much smaller than the ~20 % increase in applied field (i.e. 10s of Oe) noted earlier to be required to explain the experimental data. We additionally performed calculations where we replaced $K_1$ with $K_{defect}$, ranging between $0.4K_1$ and $1.5K_1$ and obtained effective fields of a similar magnitude, suggesting that the size of these effects would not be substantially amplified by the change of magnetic properties within the defect site. Indeed, Figure 6 shows that the strength of the magnetoelastic interactions (as characterized by $B_1 e$) would need to be increased by two orders of magnitude to create changes in the depinning probability similar to that observed in the experimental data. This result is not unexpected because any spatial gradient of the magnetoelastic terms for these long wavelength (32 μm) waves will be negligible over the width of a DW.

The modulation of the pining barrier, however, shows significant changes in the depinning probability. The combined out-of-plane and magnetoelastic anisotropies may be written as:

$$E_K + E_{ME} = -(K_1 + B_1 e \sin(\omega t) \sin(kx))\alpha_z^2 = -K_{net}(x,t)\alpha_z^2 \quad (7)$$

where $K_1$ is the material's out-of-plane anisotropy constant and $K_{net}(x,t)$ is the net out-of-plane anisotropy constant resulting from the combined effects of surface anisotropy and magnetoelastic anisotropy. SAWs result in a strain induced spatial and temporal modulation of the stripes's out-of-plane anisotropy that can rotate the direction of magnetization of ferromagnetic microstructures [16], [17].

Here, the SAW acts to modulate the pinning potential, as characterized by $E_0$ and $H_0$. In the presence of SAW, $K_1$ and $K_{defect}$ are replaced by $K_{1,net}(x,t)$ and $K_{defect,net}(x,t)$ as defined by Equation (5). Equation (6) then becomes:

$$E_H(x,t) = E_0(x,t)\left(1 - \frac{H}{H_0(x,t)}\right) \quad (8)$$

This produces a time varying modulation of the energy barrier against depinning, resulting in a time varying $\tau$. To calculate the probability of the DW depinning within a single period of the SAW we use $\tau(x,t)$ to numerically integrate Equation (1). We then use this single-cycle probability to extrapolate the probability of the DW depinning within a fixed time interval of SAW excitation.

We note that the barrier modulation model contains two free parameters, $K_{defect}$ and $l_y$ of which there will be many combinations that produce a value of $E_0$ that agrees with that determined from the experimental data (Table 1). In the results we present here we have treated $l_y$ as a fitting parameter, which is then used to uniquely determine the value of $K_{defect}$.

Our calculations use typical parameters for Co/Pt multilayers: $K_1 = 0.75$ MJ/m$^3$ [41], $M_s = 670$ kA/m [42], exchange stiffness $A_{ex} = 7.5$ pJ/m [43], $B_1 = -15.9 \times 10^6$ N/m$^2$ [36] and $d = 3.9$ nm (i.e. the total thickness encompassing the stripe's magnetic layers). Our calculations of the impedance mismatch between the IDTs and the signal generator (see Supplementary Information) indicate that a 5V signal at the generator corresponds to a strain of $e = 0.42 \times 10^{-3}$. The fits however require a higher value of strain, $e = 1 \times 10^{-3}$ for the maximum applied value of $V_{SAW} = 4.94$ V. The high strains required for the model may in part be due to the simple nature of the model, but it is also possible that multiple reflections between the two IDTs could increase the standing wave amplitude. We apply the models to the data in a manner that maximizes their influence of the SAW i.e. by placing the defect site at a node of the SAW standing wave for the effective field model, and at an antinode for the barrier modulation model. In reality the strength of the SAWs influence will vary depending on defect position, but we consider our approach appropriate for understanding whether the magnitude of the effects are sufficient to explain the experimental data.

The model produces reasonable fits to the data in all cases, with $l_y$ taking values ~$\pi\Delta$ (Table 1). We therefore conclude that this is a possible origin of the experimentally observed effects. Furthermore, the model allows us to understand the lack of a clear positional dependence of the ability of the standing SAW to affect depinning (Figure 4(c)), because SAW induced depinning will depend not only on the position of the defect relative to the SAWs nodes and antinodes, but also on the depth, edge profile and spatial extent of the defect sites.

Our conclusions here must be carefully caveated. Whilst the barrier modulation model can reproduce the experimental data relatively well, the best fit values of $l_y$and $K_{defect}$ imply that the stripe's defect sites are of very limited spatial extent and exhibit a large reduction in local anisotropy. In fact, our model suggests that the SAW can only substantially affect depinning if the reduced anisotropy of the defect lies close to the transition between out-of-plane and in-plane magnetization. This can be seen in the relative homogeneity of the fitted values of $K_{defect}$ in Table 1. However, our model is simple and neglects many potential phenomena including the elasticity of the DW, other possible contributions to the pinning potential (e.g. localized variations in $M_s$, $A_{ex}$), subtleties of DW structure and the more complex stress profiles of SAWs propagating through anisotropic and piezoelectric substrates such as $LiNbO_3$. It is possible that inclusion of these effect in the model might allow for a process that is less critically balanced.

The modeling indicates that SAW assisted depinning of DWs is consistent with a shrinking DW potential well, rather than the usual tilting that results from effective fields. This is significant because raising the pinning potential to zero will effectively alter the depinning process from stochastic to deterministic. In addition, the SAW provides a low power route to depinning. Calculations (see Supplementary Information) indicate that at the highest voltage, the total power going into the pair of IDTs is 67 mW. This power is distributed over the entire 225 μm length of the IDTs and only a small fraction is incident on each [Co/Pt] stripe, proportional to the width of the stripes. So, for example, a 5 μm wide strip is subject to a total of 67*(5 μm/225 μm)=1.49mW, for a power density of 1.3 W/mm$^2$. This compares very favorably to current driven depinning, with power densities that are hundreds of times higher. The power and power density for current induced depinning in a Co/Ni-based spin valve [9] in the presence of a magnetic field are 312 mW and 340W/mm$^2$, respectively. Current injection to depin DWs from patterned notches in CoPt nanowires [44] require power and power densities of 1.75 mw and 875W/mm$^2$, respectively.

In conclusion, we have shown that high frequency strain waves assist in the depinning of magnetic domain walls, increasing the probability of depinning by factors ranging between 4 and 9. The effect is proportional to strain and equivalent to a 20% increase in driving stimulus at an applied voltage of 5V. Simple models have been used to examine the origin of these effects and suggest that the SAW enhanced depinning is the result of magnetoelastic modulation of energy wells presented by defect sites. Our results indicate that SAW generated strain are a viable, low power method for effectively depinning DWs from strong pinning sites.

See Supplementary material for the amplitude of strain wave and power to IDTs, the effective field model, Figures S1 for the complete analysis with pulse width, field and SAW for $S_3$ (4 µm) and $S_9$ (5 µm) and Figure S2 for the DW velocity as a function of the field and SAW voltage.

Acknowledgement

This work was supported by NSF (DMR-1409622) and NSF Nebraska MRSEC (DMR-1420645). The research was performed in part in the Nebraska Nanoscale Facility: National Nanotechnology Coordinated Infrastructure and the Nebraska Center for Materials and Nanoscience, which are supported by the National Science Foundation under Award ECCS: 1542182, and the Nebraska Research Initiative. EM and TH acknowledge support from EPSRC grant EP/T018399/1. TH acknowledges useful discussions with K. Livesey.

Data Availability

The data that support the findings of this study are available from the corresponding author upon reasonable request.

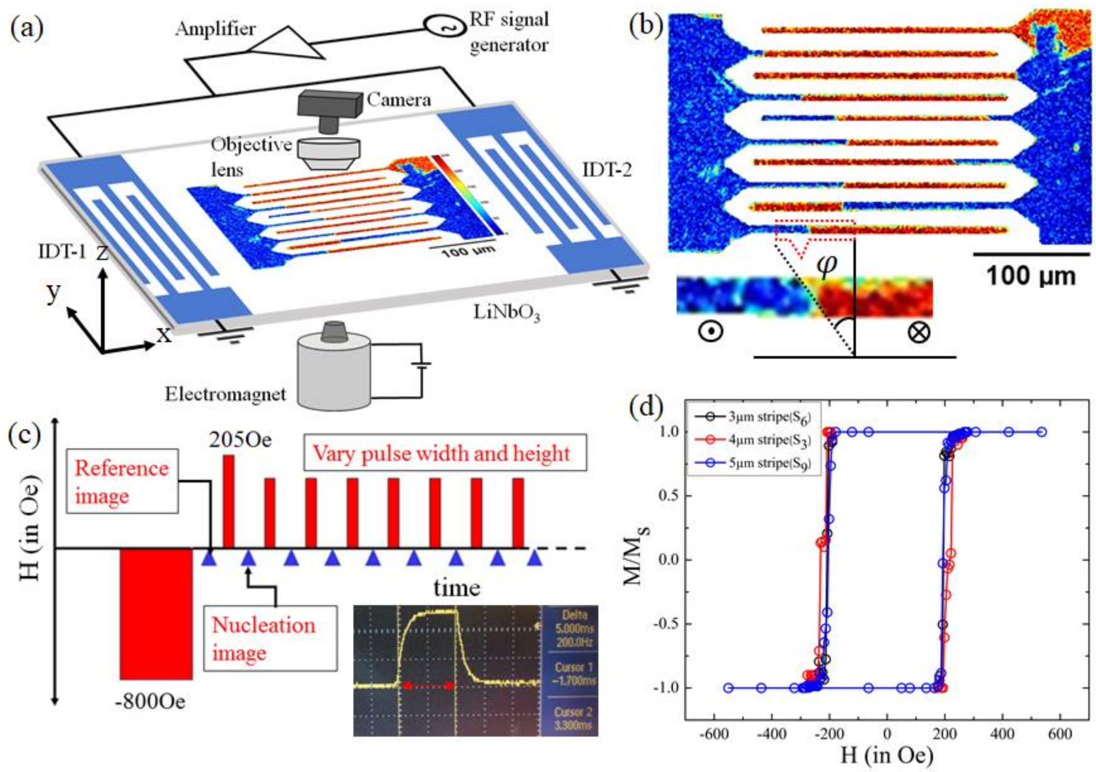


*Figure 1. (a) Schematic of the magnetic stripes, IDTs, MOKE microscope and rf electronics. (b) MOKE image showing red and blue magnetic domains. Inset is a magnified view of the domain wall. (c) The pulse train used to drive domain walls along the stripes. Inset is an oscilloscope trace of a 5ms pulse to the electromagnet measured across a 50 Ohm resistor in series with the electromagnet. Scale bar is 5ms. (d) MOKE measurements of hysteresis loops for three stripes of differing widths: 3µm ($S_6$), 4µm ($S_3$) and 5µm ($S_9$).*

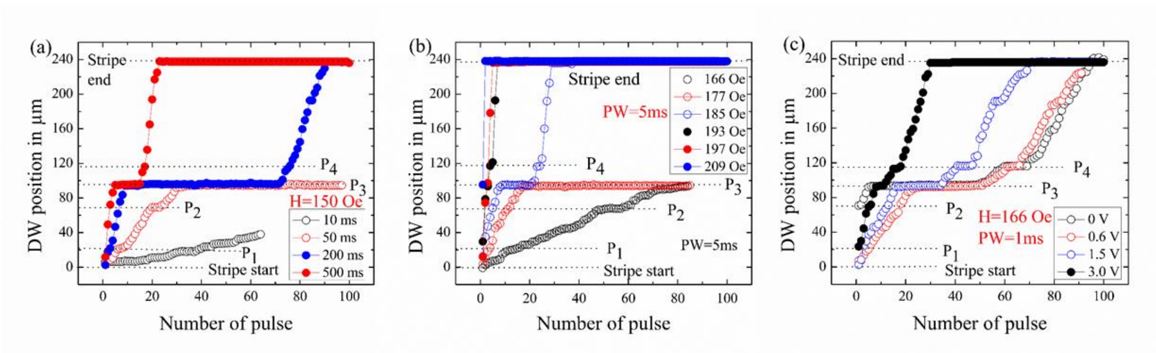


*Figure 2. The domain wall position as a function of the number of pulses for the 3μm stripe (a) for varying pulse widths at a constant field of 150 Oe (b) for varying magnetic fields at a constant pulse width of 5ms and (c) for varying SAW voltages at a fixed field of 166 Oe with a pulse width of 1ms.*

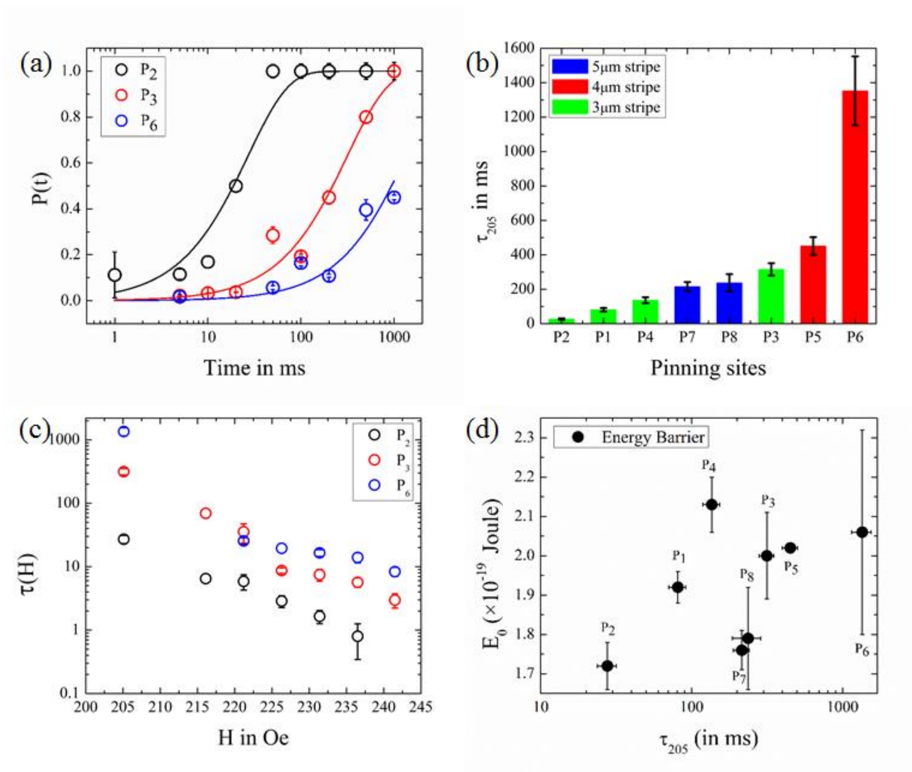


*Figure 3. (a) Depinning probability, $P(t)$, for three representative pinning sites as a function of pulse width at a field value of 205 Oe. The solid lines are fits based on Equation (1). (b)Bar graph of the characteristic depinning times, $\tau_{205}$, for each pinning site, ranging from a low of 0.03 s to a high of 1.4 s. (c) The characteristic depinning time $\tau$, as a function of magnetic field. (d) The pinning site energy barrier $E_0$ for each pinning site plotted as function of $\tau_{205}$ which is a measure of the strength of the pinning site.*

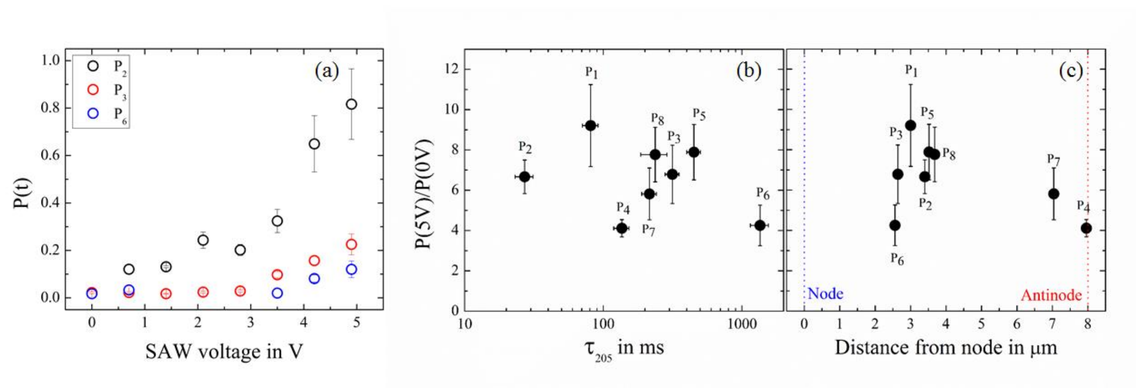


*Figure 4. (a) The depinning probability, $P(t)$, as a function of increasing SAW voltage for three representative pinning sites. The ratio of depinning probability at 5V to 0V for each pinning site as a function of (b) $\tau_{205}$ and (c) distance from the nearest node. The dashed blue (red) line represents the nearest node (antinode).*

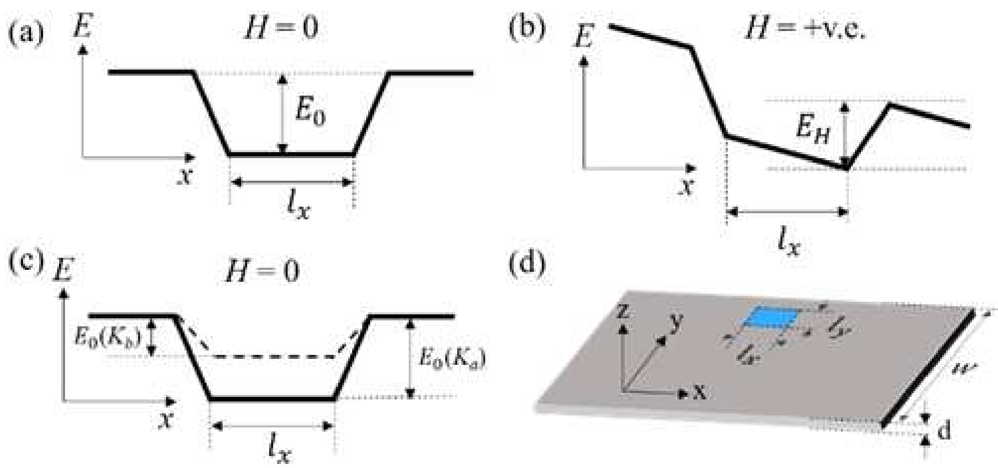


*Figure 5: (a) Illustration of the defect energy wells assumed in our models. (b) Effect of an applied field on the defect energy wells. (c) Illustration of how the shape of a modeled energy well is altered by changes in local anisotropy. (d) Illustration of the geometry of nanowire and defect sites.*

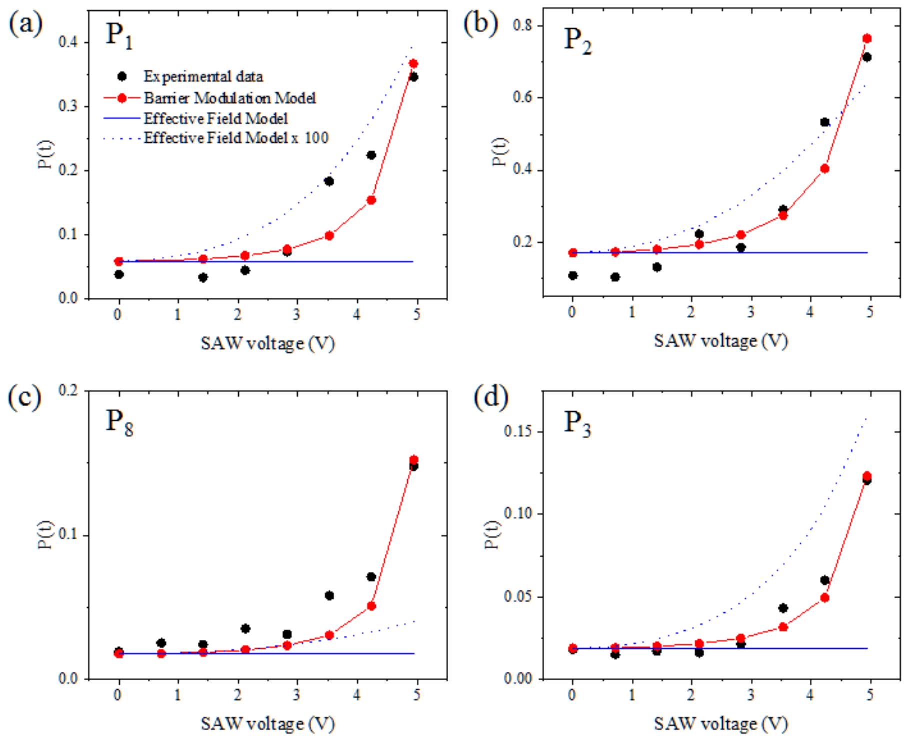


*Figure 6: Fits of the effective field model (blue line) and barrier modulation model (red line) to experimental measurements of depinning probability as a function SAW voltage (black circles). Data/fits are shown for defect sites (a) $P_1$, (b) $P_2$, (c) $P_8$ and (d) $P_3$. The dashed blue line shows the predictions of the effective field model when the strength of magnetoelastic interactions are enhanced by two orders of magnitude.*

## REFERENCES

[1] D. Atkinson, D. A. Allwood, G. Xiong, M. D. Cooke, C. C. Faulkner, and R. P. Cowburn, "Magnetic domain-wall dynamics in a submicrometre ferromagnetic structure," *Nat. Mater.*, vol. 2, no. 2, pp. 85–87, 2003.

[2] S. H. Yang, K. S. Ryu, and S. Parkin, "Domain-wall velocities of up to 750 m s-1 driven by exchange-coupling torque in synthetic antiferromagnets," *Nat. Nanotechnol.*, vol. 10, no. 3, pp. 221–226, 2015.

[3] P. Sethi *et al.*, "Bi-directional high speed domain wall motion in perpendicular magnetic anisotropy Co/Pt double stack structures," *Sci. Rep.*, vol. 7, no. 1, pp. 1–8, 2017.

[4] G. Winkler, A. Kobs, A. Chuvilin, D. Lott, A. Schreyer, and H. P. Oepen, "On the variation of magnetic anisotropy in Co/Pt(111) on silicon oxide," *J. Appl. Phys.*, vol. 117, no. 10, p. 105306, 2015.

[5] D. Wu, S. Chen, Z. Zhang, B. Ma, and Q. Y. Jin, "Enhancement of perpendicular magnetic anisotropy in Co/Ni multilayers by in situ annealing the Ta/Cu under-layers," *Appl. Phys. Lett.*, vol. 103, no. 24, p. 242401, 2013.

[6] B. Zhang *et al.*, "Energy-Efficient Domain-Wall Motion Governed by the Interplay of

Helicity-Dependent Optical Effect and Spin-Orbit Torque," *Phys. Rev. Appl.*, vol. 11, no. 3, p. 034001, 2019.

[7] S. B. Choe, D. H. Kim, K. S. Ryu, H. S. Lee, and S. C. Shin, "Direct observation of Barkhausen effect in strip-patterned ferromagnetic CoPd multilayer films," *J. Appl. Phys.*, vol. 99, no. 10, 2006.

[8] A. J. Schellekens, A. Van Den Brink, J. H. Franken, H. J. M. Swagten, and B. Koopmans, "Electric-field control of domain wall motion in perpendicularly magnetized materials," *Nat. Commun.*, vol. 3, no. May, pp. 845–847, 2012.

[9] S. Le Gall *et al.*, "Statistical study of domain-wall depinning induced by magnetic field and current in an epitaxial Co/Ni-based spin-valve wire," *Phys. Rev. B*, vol. 98, no. 2, pp. 1–9, 2018.

[10] M. Hayashi, L. Thomas, R. Moriya, C. Rettner, and S. S. P. Parkin, "Current-controlled magnetic domain-wall nanowire shift register," *Science (80-. ).*, vol. 320, no. 5873, pp. 209–211, 2008.

[11] P. M. Shepley, A. W. Rushforth, M. Wang, G. Burnell, and T. A. Moore, "Modification of perpendicular magnetic anisotropy and domain wall velocity in Pt/Co/Pt by voltage-induced strain," *Sci. Rep.*, vol. 5, pp. 1–5, 2015.

[12] A. A. Grachev, S. E. Sheshukova, S. A. Nikitov, and A. V. Sadovnikov, "Strain reconfigurable spin-wave transport in the lateral system of magnonic stripes," *J. Magn. Magn. Mater.*, vol. 515, no. July, p. 167302, 2020.

[13] A. V. Sadovnikov *et al.*, "Magnon Straintronics: Reconfigurable Spin-Wave Routing in Strain-Controlled Bilateral Magnetic Stripes," *Phys. Rev. Lett.*, vol. 120, no. 25, pp. 257203 (1–6), 2018.

[14] N. S. Gusev, A. V. Sadovnikov, S. A. Nikitov, M. V. Sapozhnikov, and O. G. Udalov, "Manipulation of the Dzyaloshinskii-Moriya Interaction in Co/Pt Multilayers with Strain," *Phys. Rev. Lett.*, vol. 124, no. 15, p. 157202, 2020.

[15] W. Yang and H. Schmidt, "Acoustic control of magnetism toward energy-efficient applications Acoustic control of magnetism toward energy-efficient applications," *Appl. Phys. Rev.*, vol. 8, no. 2, p. 021304, 2021.

[16] S. Davis, J. A. Borchers, B. B. Maranville, and S. Adenwalla, "Fast strain wave induced magnetization changes in long cobalt bars: Domain motion versus coherent rotation," *J. Appl. Phys.*, vol. 117, no. 6, pp. 0–10, 2015.

[17] S. Davis, A. Baruth, and S. Adenwalla, "Magnetization dynamics triggered by surface acoustic waves," *Appl. Phys. Lett.*, vol. 97, no. 23, p. 232507, 2010.

[18] W. Edrington, U. Singh, M. A. Dominguez, J. R. Alexander, R. Nepal, and S. Adenwalla, "SAW assisted domain wall motion in Co/Pt multilayers," *Appl. Phys. Lett.*, vol. 112, no. 5, p. 052402, 2018.

[19] A. Adhikari and S. Adenwalla, "Surface acoustic waves increase magnetic domain wall velocity," *AIP Adv.*, vol. 11, no. 1, p. 015234, 2021.

[20] W. Li, B. Buford, A. Jander, and P. Dhagat, "Acoustically assisted magnetic recording: A new paradigm in magnetic data Storage," *IEEE Trans. Magn.*, vol. 50, no. 3, pp. 37–40, 2014.

[21] L. Thevenard *et al.*, "Strong reduction of the coercivity by a surface acoustic wave in an

out-of-plane magnetized epilayer," *Phys. Rev. B*, vol. 93, no. 14, pp. 1–5, 2016.

[22] L. Thevenard *et al.*, "Precessional magnetization switching by a surface acoustic wave," *Phys. Rev. B*, vol. 93, no. 13, p. 134430, 2016.

[23] D. Castilla *et al.*, "Magnetization process of a ferromagnetic nanostrip under the influence of a surface acoustic wave," *Sci. Rep.*, vol. 10, no. 1, pp. 1–8, 2020.

[24] M. Weiler *et al.*, "Elastically driven ferromagnetic resonance in nickel thin films," *Phys. Rev. Lett.*, vol. 106, no. 11, pp. 1–4, 2011.

[25] M. Weiler, H. Huebl, F. S. Goerg, F. D. Czeschka, R. Gross, and S. T. B. Goennenwein, "Spin pumping with coherent elastic waves," *Phys. Rev. Lett.*, vol. 108, no. 17, pp. 1–5, 2012.

[26] J. Dean, M. T. Bryan, J. D. Cooper, A. Virbule, J. E. Cunningham, and T. J. Hayward, "A sound idea: Manipulating domain walls in magnetic nanowires using surface acoustic waves," *Appl. Phys. Lett.*, vol. 107, no. 14, p. 142405, 2015.

[27] C. Wuth, P. Lendecke, and G. Meier, "Temperature-dependent dynamics of stochastic domain-wall depinning in nanowires," *J. Phys. Condens. Matter*, vol. 24, no. 2, p. 024207, 2012.

[28] W. Wernsdorfer *et al.*, "Measurements of magnetization switching in individual nickel nanowires," *Phys. Rev. B*, vol. 55, no. 17, pp. 11552–11559, 1997.

[29] D. Makarov *et al.*, "Nonepitaxially grown nanopatterned Co-Pt alloys with out-of-plane magnetic anisotropy," *J. Appl. Phys.*, vol. 106, no. 11, pp. 1–7, 2009.

[30] D. Makarov *et al.*, "Nanopatterned CoPt alloys with perpendicular magnetic anisotropy," *Appl. Phys. Lett.*, vol. 93, no. 15, pp. 1–4, 2008.

[31] J. C. Read, P. M. Braganca, N. Robertson, and J. R. Childress, "Magnetic degradation of thin film multilayers during ion milling," *APL Mater.*, vol. 2, no. 4, p. 046109, 2014.

[32] G. Blanchet and M. Charbit, *Digital Signal and Image Processing using MATLAB®*. 2013. (New York: Wiley) https://doi.org/10.1002/9780470612385.

[33] T. Ferreira and W. Rasband, "ImageJ User Guide-IJ1.46," 2010-2012. https://imagej.nih.gov/ij/docs/guide

[34] M. P. Sharrock, "Time dependence of switching fields in magnetic recording media," *J. Appl. Phys.*, vol. 76, no. 10, pp. 6413–6418, 1994.

[35] M. Spindler, B. Uhlig, S. B. Menzel, C. Huck, T. Gemming, and J. Eckert, "Local temperature determination in power loaded surface acoustic wave structures using Raman spectroscopy," *J. Appl. Phys.*, vol. 114, no. 16, 2013.

[36] M. Komelj and M. Fähnle, "Nonlinear magnetoelastic effects in ultrathin epitaxial FCC Co(0 0 1) films: An ab initio study," *J. Magn. Magn. Mater.*, vol. 224, no. 1, pp. 1–4, 2001.

[37] P. Manchanda, U. Singh, S. Adenwalla, A. Kashyap, and R. Skomski, "Strain and stress in magnetoelastic Co-Pt multilayers," *IEEE Trans. Magn.*, vol. 50, no. 11, pp. 2–5, 2014.

[38] R. Ploessl, J. N. Chapman, M. R. Scheinfein, J. L. Blue, M. Mansuripur, and H. Hoffmann, "Micromagnetic structure of domains in Co/Pt multilayers. I. Investigations of wall structure," *J. Appl. Phys.*, vol. 74, no. 12, pp. 7431–7437, 1993.

[39] J. J. W. Goertz, G. Ziemys, I. Eichwald, M. Becherer, H. J. M. Swagten, and S. Breitkreutz-V. Gamm, "Domain wall depinning from notches using combined in- and out-

of-plane magnetic fields," *AIP Adv.*, vol. 6, no. 5, p. 056407, 2016.

[40] M. D. Dejong and K. L. Livesey, "Analytic theory for the switch from Bloch to Néel domain wall in nanowires with perpendicular anisotropy," *Phys. Rev. B*, vol. 92, no. 21, pp. 1–12, 2015.

[41] W. W. Lin, H. Sang, B. You, Z. S. Jiang, and G. Xiao, "Angular dependence of magnetic properties in Co/Pt multilayers with perpendicular magnetic anisotropy," in *International Journal of Modern Physics B*, 2005, vol. 19, no. 15–17, pp. 2562–2567.

[42] A. Barman, S. Wang, O. Hellwig, A. Berger, E. E. Fullerton, and H. Schmidt, "Ultrafast magnetization dynamics in high perpendicular anisotropy [CoPt]n multilayers," *J. Appl. Phys.*, vol. 101, no. 9, pp. 10–13, 2007.

[43] J. H. Shim *et al.*, "Ultrafast dynamics of exchange stiffness in Co/Pt multilayer," *Commun. Phys.*, vol. 3, no. 1, pp. 1–8, 2020.

[44] S. J. Noh, Y. Miyamoto, N. Hayashi, J. S. Lee, and Y. K. Kim, "Magnetic domain wall motion by current injection in CoPt nanowires consisting of notches," *Solid State Commun.*, vol. 152, no. 12, pp. 1004–1007, 2012.